

Dyons near the transition temperature in lattice QCD

V. G. Bornyakov

*Institute for High Energy Physics NRC “Kurchatov Institute”, 142281 Protvino, Russia,
Institute of Theoretical and Experimental Physics, 117259 Moscow, Russia
School of Biomedicine, Far East Federal University, 690950 Vladivostok, Russia*

E.-M. Ilgenfritz

Joint Institute for Nuclear Research, BLTP, 141980 Dubna, Russia

B. V. Martemyanov

*Institute of Theoretical and Experimental Physics, 117259 Moscow, Russia
National Research Nuclear University MEPhI, 115409, Moscow, Russia
Moscow Institute of Physics and Technology, 141700, Dolgoprudny, Moscow Region, Russia*

M. Müller-Preussker

Humboldt-Universität zu Berlin, Institut für Physik, 12489 Berlin, Germany

(Dated: April 29, 2022)

We study the topological structure of QCD by cluster analysis. The fermionic topological charge density is constructed from low lying modes of overlap Dirac operator for three types of temporal boundary conditions for fermion field. This gives the possibility to mark all three dyon constituents of KvBLL caloron in gluonic fields. The gluonic topological charge density is appearing in the process of overimproved gradient flow process stopped at the moment when it maximally matches the fermionic topological charge density. This corresponds to the smearing of gluonic fields up to the scale set by dyon size. The time-like Abelian monopoles and specific KvBLL pattern of Polyakov line correlate with topological clusters.

PACS numbers: 11.15.Ha, 12.38.Gc, 12.38.Aw

Keywords: Lattice gauge theory, overlap Dirac operator, caloron, dyon

I. INTRODUCTION

Two basic properties of QCD are confinement (of quarks and gluons) and the spontaneous breaking of chiral symmetry at low temperature and density. Both properties are believed to be intimately connected with each other and to originate from a certain complex structure of the QCD vacuum state, the simplest manifestations of which being condensates of gluon and quark fields. The field fluctuations contributing to these condensates are, however, space-time and scale dependent. One of the aims of Lattice Gauge Theory is to reveal the corresponding structures. One school of thought claims that - at the infrared scale - the origin of both mechanisms can be traced back to semiclassical objects of QCD. These objects either disappear or change their properties at high temperature, where the quark-gluon plasma phase appears.

Today it is commonplace to say that the instanton mechanism is able to explain chiral symmetry breaking while it fails to provide a mechanism for confinement. Without further sophistications this is definitely correct for the instanton gas or liquid. Constituent dyons of Kraan-van Baal-Lee-Lu (KvBLL) calorons [1–3], however, are as good as instantons in explaining chiral symmetry breaking. Calorons with their dyon “substructure” give some room to

reproduce certain features of confinement (Polyakov loop correlators, spatial string tension, vortex and/or monopole percolation) which was the reason why people expected for decades that “instanton quarks” might solve the confinement problem. Moreover, dyons when considered as rarefied gas, either without interaction or with Coulomb-like interaction, give confining behavior for space-like Wilson loops and for correlators of Polyakov loops. The history of this idea ranges from the 70’s to the recent past [4–8].

The modelling of dyon ensembles with interaction has got even more attraction recently [9–14]. Therefore, it is of some interest to search for dyons in thermal Monte Carlo configurations (representing lattice gauge fields at different temperatures) in order to assess the relevance of these models and in order to eventually observe dyons clustering into caloron-like quasiclassical configurations.

The caloron with nontrivial holonomy [1–3] has the remarkable property that the single zero mode of the Dirac operator is able to locate on distinct constituent dyons [15, 16], depending on the temporal boundary condition (b.c.) applied to the Dirac operator if it possesses improved chiral properties.

Inspired by the KvBLL solutions, for a subset of thermal lattice configurations of fixed total topological charge $Q = \pm 1$ (created below and above T_{dec}) the change of the single zero mode’s localization with

the change of b.c. was observed by Gattringer et al. [17, 18] and interpreted in the caloron picture, ignoring other topological features of these configurations. In the case of $SU(2)$ and $SU(3)$ lattice gauge theory it has been seen that this property of mobility (and changing degree of localization) is shared also by a band of near-zero modes of the overlap Dirac operator [19–22].

Thus, not only the set of zero modes reflecting the total topological charge of the gluonic field, but the band of low lying modes of the overlap Dirac operator identified with different boundary conditions can be used as an effective tool to detect distinct topological objects. This direct insight in Monte Carlo configurations of lattice gauge fields (without cooling or smearing) is restricted, however, to a corresponding scale set by the eigenvalues. In the present paper we will see to what extent this technique leads us to the three dyons making up one “instanton” (caloron) of QCD.

In Section II we introduce the lattice set-up in which the ensembles of gauge fields which we are going to analyze have been generated in lattice QCD with $N_f = 2$ dynamical flavors. In Section III we define all the topologically relevant lattice observables employed later on for the analysis. Then, in Section IV the concrete case of $N_f = 2$ lattice QCD is considered at two temperatures, at the crossover T_χ (ensemble I) and at $T = 1.06T_\chi$ (ensemble II). The fermionic topological charge density was constructed with the help of low lying modes of overlap Dirac operator computed for three types of temporal boundary conditions.

This is the point where two new ideas compared to the previous papers (dealing with $SU(3)$ gluodynamics) are introduced. (i) Again, in addition to antiperiodic boundary conditions for the overlap fermions, two other boundary conditions are employed in order to construct topological densities for each type of boundary conditions. Here, however, not the number of pairs of non-zero modes is fixed for all boundary conditions, but the eigenvalue cutoff is fixed. We consider two cutoffs at two temperatures. (ii) In order to characterize the configurations by the gluonic topological charge density, the technique of gradient flow has replaced the procedure of cooling that was previously in use. The stopping criterion is now set by the maximal approximation of the fermionic topological charge density by the gluonic one. This is how the gluonic topological density depends on the chosen cutoff scale.

It will turn out that in this way all UV fluctuations are removed, up to the size of dyons that we are searching for.

Finally, the properties of the clusters of the three fermionic topological densities under consideration are studied as well as their correlations among each other, correlations to the local holonomy and to the Abelian monopoles from the Maximally Abelian Gauge con-

struction.

In Section V we shall draw our conclusions.

II. LATTICE SETTING FOR THE THERMAL ENSEMBLES

We continue our study of topological objects in $SU(3)$ gauge theory in the case of QCD (with dynamical quarks). We have analyzed gauge field configurations generated with the Wilson gauge action S_W and $N_f = 2$ dynamical flavors of nonperturbatively $O(a)$ improved Wilson fermions (clover fermions). The configurations had been produced long ago by the DIK collaboration [23, 24] using the “Berlin QCD” code (BQCD) [25]. The improvement coefficient c_{SW} had been determined nonperturbatively [26]. The lattice spacing and pion mass had been determined by interpolation of $T = 0$ results obtained by QCDSF collaboration [27]. We have analysed configurations produced on lattices with temporal extent $L_\tau = 8$ and spatial sizes $L_s = 16$ (ensemble I of 50 configurations at $T = T_\chi$) and $L_\tau = 8$ and $L_s = 24$ (ensemble II of 50 configurations at $T = 1.06T_\chi$). The DIK collaboration had scanned the temperature T at fixed β -value by changing the Wilson fermion hopping parameter κ . In other words, the quark mass was not kept constant. The chiral crossover temperature $T_\chi \approx 230$ MeV was determined in Refs. [23, 24] at a corresponding pion mass value of $O(1 \text{ GeV})$.

In Ref.[28] we have investigated the T -dependence of the topological susceptibility throughout the interval $[0.85T_\chi, 1.26T_\chi]$ by overimproved cooling applied to ensembles of 500 or 200 configurations. We have there confronted the T -dependence with the case of pure $SU(3)$ Yang-Mills theory (with Wilson action).

For the two temperatures $T = T_\chi$ and $T = 1.06T_\chi$, that we are going to reinvestigate here with overlap fermions with respect to details of the space-time topological structure (however for a smaller subensemble of 50 configurations each), we recall the topological susceptibility we have found in Ref.[28]: ensemble I (500 configurations, overimproved cooling), $\chi_{\text{top}} = (0.6 \pm 0.05)T_\chi^4$; ensemble II (200 configurations, overimproved cooling), $\chi_{\text{top}} = (0.3 \pm 0.03)T_\chi^4$.

III. TOPOLOGICALLY RELEVANT OBSERVABLES

We use in our analysis the following instruments (observables):

- local holonomy and its trace (the Polyakov loop),
- improved gluonic topological charge,

- Abelian monopoles revealed by Abelian projection after transforming gauge field to the Maximal Abelian Gauge (MAG).

All these quantities are computed after gradient flow (in close correspondence to over-improved cooling). We also use

- the fermionic topological charge density (and its UV-filtered version) including its dependence on the temporal boundary conditions imposed on overlap fermions.

The importance and usefulness of the finite-temperature holonomy (considered globally to distinguish the phases of the theory and locally to distinguish the dyonic constituents or “instanton quarks”) for the topological structure studies was recognized only through the discovery of the KvBLL-caloron solutions [1–3].

A. Holonomy

The local holonomy is defined as a product of time-like links

$$P(\vec{x}) = \prod_{x_0=1}^{N_\tau} U_0(\vec{x}, x_0) \quad (1)$$

$P(\vec{x})$ has eigenvalues

$$\lambda_k(\vec{x}) = \exp(i2\pi\mu_k(\vec{x})) . \quad (2)$$

The positions in space of the dyon constituents of KvBLL calorons are determined by the condition that two of these eigenvalues coincide (cf. Appendix in [21]). We use this property to localize (anti)dyons in unsmoothed lattice field configurations.

The asymptotic holonomy of KvBLL calorons (after a suitable constant gauge transformation)

$$\mathcal{P}_\infty \equiv \lim_{|\vec{x}| \rightarrow \infty} P(\vec{x}) = \exp[2\pi i \text{diag}(\mu_1, \mu_2, \mu_3)], \quad (3)$$

is characterized by the eigenphases, three real and ordered numbers $\mu_1 \leq \dots \leq \mu_3 \leq \mu_4 \equiv 1 + \mu_1$ fulfilling $\mu_1 + \mu_2 + \mu_3 = 0$. The set of eigenphases eventually determines the masses of well-separated dyon constituents via $8\pi^2\nu_m$, where $\nu_m \equiv \mu_{m+1} - \mu_m$ (cf. Appendix in [21]).

The trace of $P(\vec{x})$ is the gauge invariant complex-valued Polyakov loop

$$L(\vec{x}) = \frac{1}{3} \text{Tr} P(\vec{x}) . \quad (4)$$

Its value can be represented as a point in the Weyl plot in the complex plane, see Fig. [refplincl](#) in Section IV.

For $SU(3)$, when two eigenvalues of the local holonomy are equal, respective Polyakov loop is represented

by the point in the periphery of the Weyl plot. If all three eigenvalues coincide, the holonomy is an element of the center group

$$P(\vec{x}) = z_i \cdot I , \quad (5)$$

where

$$z_i \in \{1, \exp(2\pi i/3), \exp(-2\pi i/3)\}.$$

The expectation value of the spatially averaged Polyakov loop (V_3 is the spatial volume) :

$$\bar{L} = \frac{1}{V_3} \sum_{\vec{x}} L(\vec{x}) . \quad (6)$$

is an order parameter of the deconfinement transition in pure Yang-Mills gauge theory, signalling the breaking of the center symmetry. In presence of dynamical fermions, this symmetry is – at best – only approximate, even at low temperature.

B. MAG and Abelian monopoles definitions

We use the definition of MAG introduced for lattice $SU(N)$ theory in [29] and later specified for the $SU(3)$ group in [30]. The MAG is fixed by maximizing the functional

$$F[U] = \frac{1}{12V} \sum_{x,\mu} [|(U_\mu(x))_{11}|^2 + |(U_\mu(x))_{22}|^2 + |(U_\mu(x))_{33}|^2] \quad (7)$$

with respect to local gauge transformations g of the lattice gauge field,

$$U_\mu(x) \rightarrow U_\mu^g(x) = g(x)^\dagger U_\mu(x) g(x + \hat{\mu}) . \quad (8)$$

Alternative definitions of the MAG condition for the $SU(3)$ group were introduced in [31] and were studied further in [32]. To maximize the functional eq. (7) we use the simulated annealing algorithm which was found very much effective to fight the problem of Gribov copies [33]. For $SU(3)$ gauge group it was first used in [34], see also [35] for details of its implementation to the case of the $SU(3)$ gauge group. After fixing to MAG the Abelian fields $u_\mu(x) \in U(1) \times U(1)$ are determined as a result of the Abelian projection described in [29].

The monopole currents $j_\mu^{(a)}(*x)$ are defined [29] on links of the dual lattice and satisfy the current conservation law for every a separately:

$$\sum_\mu \partial_\mu^- j_\mu^{(a)}(s) = 0, \quad a = 1, 2, 3. \quad (9)$$

Additionally

$$\sum_{a=1}^3 j_\mu^{(a)}(x) = 0, \quad (10)$$

i.e. only two currents are independent.

C. The gluonic definition of the topological density

The definition of topological charge density is

$$q(x) = \frac{1}{16\pi^2} \text{Tr}(F_{\mu\nu}(x) \tilde{F}_{\mu\nu}(x)) \quad (11)$$

were

$$\tilde{F}_{\mu\nu}(x) = \frac{1}{2} \epsilon_{\mu\nu\lambda\sigma} F_{\lambda\sigma}(x). \quad (12)$$

The lattice gluonic topological charge density uses field strength definition of $F_{\mu\nu}(x)$ as a ‘‘clover’’ average over the traceless antihermitean part of all four plaquettes within the $\mu\nu$ plane with sidelength $n = 1$ placed around a site x while kept untraced in that site x . The improved topological charge density [36] extends this construction to quadratic loops of sizes $n = 2, 3$ which are added with appropriate weights. The improved topological charge and corresponding action (in units of the one-instanton action S_{inst}) are then defined as

$$Q_{\text{glue}} = \sum_x \text{Tr}(F_{\mu\nu}(x) \tilde{F}_{\mu\nu}(x))/(16\pi^2), \quad (13)$$

$$S/S_{\text{inst}} = \sum_x \text{Tr}(F_{\mu\nu}(x) F_{\mu\nu}(x))/(16\pi^2). \quad (14)$$

D. Over-improved gradient flow

Gradient flow is an advanced method to remove quantum fluctuations up to a certain ‘‘diffusion’’ scale from given lattice field configurations created in the course of Monte Carlo simulations [51]. The gradient flow effectively results also in a minimization of the action in the ‘‘direction’’ of steepest descent in configuration space [37–39]. Proposed by Lüscher for the Wilson (one-plaquette) action, the gradient flow can be defined with respect to different gluonic actions, of which Wilson flow realizes the simplest case. In our case, we propose to use the gradient flow with respect of an action of the form

$$S(\epsilon) = \sum_{x,\mu\nu} \frac{4-\epsilon}{3} \text{Re Tr} (1 - U_{x,\mu\nu}) + \sum_{x,\mu\nu} \frac{1-\epsilon}{48} \text{Re Tr} (1 - U_{x,\mu\nu}^{2 \times 2}), \quad (15)$$

which reduces to the Wilson action in the case $\epsilon = 1$. The so-called over-improved action [40] corresponds to $\epsilon = -1$. Expanding in powers of lattice spacing a , one finds that the lattice action includes now higher dimension operators:

$$S(\epsilon) = \sum_{x,\mu\nu} a^4 \text{Tr} \left[\frac{1}{2} F_{\mu\nu}^2(x) - \frac{\epsilon a^2}{12} (D_\mu F_{\mu\nu}(x))^2 \right] + O(a^8). \quad (16)$$

For a discretized continuum instanton of size ρ this provides corrections of order a/ρ :

$$S(\epsilon) = 8\pi^2 \left[1 - \frac{\epsilon}{5} \left(\frac{a}{\rho} \right)^2 + \mathcal{O} \left(\left[\frac{a}{\rho} \right]^4 \right) \right] \quad (17)$$

suggesting that under cooling ρ will decrease for $\epsilon > 0$ and increase for $\epsilon < 0$. The inversion of lattice artefacts relative to the Wilson case makes topological lumps stable against the process of gradient flow.

It is worth noting that standard gradient flow or Wilson flow [37–39] ($\epsilon = 1$) can be mapped one-to-one [41] to standard Wilson cooling. From Fig.(1) it is seen that the same holds for over-improved gradient flow in the sense that it nicely follows over-improved cooling.

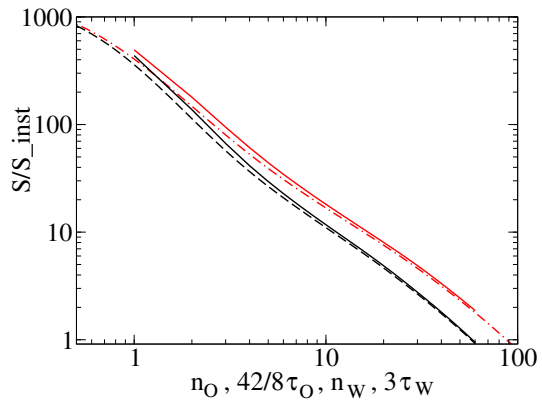


FIG. 1: The evolution of action (14) (in instanton units) with Wilson cooling step n_W (black line) and with Wilson flow time $3\tau_W$ (black dashed line) shown on the abscissa, and the variation of the same action (14) (in the same units) with overimproved cooling step n_O (red line) and with overimproved flow time $(42/8)\tau_O$ shown on the abscissa (red dash-dotted line).

E. UV filtered fermionic topological charge density

We consider the near-zero-mode (NZM) band of eigenmodes of the massless overlap operator D . We use the overlap Dirac operator D of the form [43, 44]

$$D(m=0) = \frac{\rho}{a} \left(1 + \frac{D_W}{\sqrt{D_W^\dagger D_W}} \right) = \frac{\rho}{a} (1 + \text{sgn}(D_W)), \quad (18)$$

where $D_W = M - \rho/a$, M is the hopping term of the Wilson-Dirac operator and ρ/a is a negative mass

term usually determined by optimization. The index of D , can be identified with the integer-valued topological charge Q_{over} [45]. The non-zero modes have vanishing chirality and appear in pairs with modes in the pair related by $\psi_\lambda = \gamma_5 \psi_{-\lambda}$.

For the configurations with $L_\tau = 8$ and spatial size $L_s = 16$ at $T = T_\chi$ (ensemble I of 50 configurations) we found from the average square of the number of zero modes (equal to $\langle Q^2 \rangle$) $\chi_{\text{top}} = (0.71 \pm 0.17) T_\chi^4$. For the ensemble II of 50 configurations with $L_\tau = 8$ and spatial size $L_s = 24$ at $T = 1.06 T_\chi$ we found $\chi_{\text{top}} = (0.24 \pm 0.05) T_\chi^4$. The comparison of these numbers with those of overimproved cooling reported in section II (the agreement is within 4 or 6 % for the fourth root of the susceptibility) specifies the systematical error induced by the cooling method.

The fermionic topological charge density with maximal resolution (down to the lattice spacing a) is defined in terms of the overlap Dirac operator (18) as follows

$$q(x) = -\text{tr} \left[\gamma_5 \left(1 - \frac{a}{2} D(m=0; x, x) \right) \right]. \quad (19)$$

Using the spectral representation of (19) after diagonalization in terms of the eigenmodes $\psi_\lambda(x)$ an UV filtered form of the density can be defined as a sum over narrow band of NZM

$$q_{\lambda_{\text{sm}}}(x) = - \sum_{|\lambda| < \lambda_{\text{sm}}} \left(1 - \frac{\lambda}{2} \right) \sum_c (\psi_\lambda^c(x), \gamma_5 \psi_\lambda^c(x)) \quad (20)$$

with λ_{sm} acting as an UV cutoff.

The diagonalization of the overlap operator is achieved using a variant of the Arnoldi algorithm [46]. We had at our disposal between 20 and 30 non-zero eigenmodes.

While the physical fermion sea is described by the Dirac operator implemented with antiperiodic temporal boundary conditions, for the purpose of analyzing the topological structure it is useful to diagonalize the Dirac operator subject to continuously modified temporal boundary conditions characterized by an angle ϕ ,

$$\psi(\vec{x}, x_4 + \beta) = \exp(i\phi) \psi(\vec{x}, x_4). \quad (21)$$

We have chosen three angles including the case of antiperiodic boundary condition,

$$\phi = \left\{ \begin{array}{l} \phi_1 \equiv -\pi/3 \\ \phi_2 \equiv +\pi/3 \\ \phi_3 \equiv \pi \end{array} \right\} \quad (22)$$

ensuring for a single caloron solution that the corresponding fermion zero modes become maximally localized at one, but each time at a different one of its three constituent dyons. Note that ϕ_3 corresponds to the antiperiodic boundary condition.

The construction of the UV smoothed topological charge density in terms of the eigenvalues and eigenmodes should be specifically done for the three boundary conditions:

$$q_{i, \lambda_{\text{sm}}}(x) = - \sum_{|\lambda| < \lambda_{\text{sm}}} \left(1 - \frac{\lambda}{2} \right) \sum_c (\psi_{i, \lambda}^c(x), \gamma_5 \psi_{i, \lambda}^c(x)), \quad (23)$$

where $i = 1, 2, 3$ enumerates the three boundary conditions defined by Eq. (22).

For the configurations with $L_\tau = 8$ and spatial sizes $L_s = 16$ (the ensemble I of 50 configurations at $T = T_\chi$) we take $\lambda_{\text{sm}} = 331$ MeV. This is the minimal spread of $|\lambda|$ among the 20 non-zero eigenvalues we have found per configuration (minimal with respect to all 50 configurations and 3 boundary conditions). For the configurations with $L_\tau = 8$ and spatial sizes $L_s = 24$ (the ensemble II of 50 configurations at $T = 1.06 T_\chi$) we take $\lambda_{\text{sm}} = 254$ MeV which is the minimal spread of $|\lambda|$ among 30 eigenvalues per configuration which we have determined by diagonalization. The actual number of non-zero modes falling into this interval and included into the definition Eq. (20) fluctuates from configuration to configuration because in the present analysis an eigenvalue cut-off is applied instead of a fixed number of modes.

We remark that in the case of ensemble I we have, besides of the cutoff $\lambda_{\text{sm}} = 331$ MeV, also considered the smaller cutoff $\lambda_{\text{sm}} = 254$ MeV known from ensemble II. This implies that the construction of the topological density including less non-zero modes than for the larger cutoff. This will allow us to discuss the effect of changing the cutoff for ensemble I (representing the lower temperature) and to compare between the two temperatures (applying the smaller cutoff both to ensemble I and ensemble II).

The localization of the topological charge within a given charge density filling a lattice configuration can be measured by the inverse participation ratio IPR which varies between the extremes 1 (totally delocalized) and V_4 (fully localized). It is defined as

$$\text{IPR} = V_4 \frac{\sum_x |q(x)|^2}{(\sum_x |q(x)|)^2}. \quad (24)$$

V_4 is the four dimensional volume. Any subvolume fV_4 equally filled results in $\text{IPR} = 1/f$. We have analyzed the IPR Eq. (24) of the three types of fermionic topological charge density corresponding to the three boundary conditions, at both temperatures for the same cutoff, and for the lower temperature (at T_χ) with two different cutoffs. The result is presented in Table I.

We can conclude, that at equal cutoff $\lambda_{\text{sm}} = 254$ MeV for antiperiodic boundary conditions the localization is 3-times bigger at higher temperature $T = 1.06 T_\chi$ compared to $T = T_\chi$. In addition, at the higher temperature, antiperiodic boundary conditions

type of boundary condition	ensemble I $\lambda_{\text{sm}} = 331$ MeV	ensemble I $\lambda_{\text{sm}} = 254$ MeV	ensemble II $\lambda_{\text{sm}} = 254$ MeV
1-st type b.c.	2.279(30)	2.373(36)	3.312(76)
2-nd type b.c.	2.282(29)	2.428(36)	3.259(84)
3-rd type b.c.	2.354(35)	2.493(45)	8.436(964)

TABLE I: Inverse Participation Ratio (IPR) of the fermionic topological charge density at the selected fermionic cutoffs λ_{sm} , for three types of boundary conditions.

result in a localization by a factor 2.5 stronger than the other two boundary conditions.

At the lower temperature T_χ , the lower cutoff $\lambda_{\text{sm}} = 254$ MeV leads only to a minor increase of localization by a few percent than the larger cutoff $\lambda_{\text{sm}} = 331$ MeV. The effect of changing boundary conditions is at a similar level.

We are now going to compare the fermionic topological density $q_f(x)$, truncated according to (23) with a fixed cut-off λ_{sm} and *averaged* over the boundary conditions, with the gluonic topological density $q_g(x)$ (11), provided a suitable amount of over-improved gradient flow has been applied to the gauge field configuration. Before we can compare, both topological densities should be corrected (by a shift [47]) to have a vanishing volume average,

$$q_g(x) \rightarrow q_g(x) - \bar{q}_g \quad (25)$$

and

$$q_f(x) \rightarrow q_f(x) - \bar{q}_f. \quad (26)$$

The optimal matching between the two (corrected) topological densities is achieved when the properly normalized “scalar product” between the two topological densities $q_g - \bar{q}_g$ and $q_f - \bar{q}_f$, expressed by the cosine between “direction vectors”,

$$\cos(\theta) = \frac{((q_g - \bar{q}_g), (q_f - \bar{q}_f))}{|q_g - \bar{q}_g||q_f - \bar{q}_f|} \quad (27)$$

passes a maximum. Fig.(2) shows the rise of the cosine towards the maximum for the 50 individual configurations of both ensembles, ensemble I (left panel) and ensemble II (right panel), as function of the flow time τ_O , until the flow is stopped at the maximum of the cosine.

Fig.(3) shows the step number (corresponding to a finite flow time step $\Delta\tau = 0.02$ adopted) linearly growing until the over-improved gradient flow is stopped. This necessary step number fluctuates from configuration to configuration. Let us note that the average step number (≈ 100) of the over-improved gradient flow corresponds to a flow time $\tau_O \approx 2$. This is the time required to let the diffusion length [52]

of gradient flow, $\sqrt{8\tau_O}$, grow to the size of a dyon $N_\tau/(2\pi\nu_d)$ where $\nu_d = \nu_1 = \nu_2 = \nu_3 = 1/3$. This would adequately describe the fractional charges in the case of maximally nontrivial holonomy (vanishing average Polyakov loop). This average step number is shown by a horizontal line in the left panel of Fig.(3) which represents the smoothing of the ensemble I. The averaged value of dimensionless quantity $t_O^2 \cdot \frac{1}{2}\text{Tr}(F_{\mu\nu}(x) F_{\mu\nu}(x))$ (with the dimensionful flow time $t_O = a^2\tau_O$) is equal to 0.37 (in the case of ensemble I) and 0.34 (for the ensemble II). This fits remarkably well to the mostly used stopping criterion for Wilson flow.

Fig.(4) shows for each configuration how the inverse participation ratio IPR evolves in the course of gradient flow, until the average fermionic density is optimally matched. The filling fraction f changes from $1/3$ to $1/10$ with the increase of temperature (see also the IPR for the fermionic topological charge density).

Topologically non-trivial clusters filtered out with the three truncated fermionic densities (23) (each corresponding to one type of fermionic boundary condition) will be separately considered in the following as topologically different objects (dyon candidates). Their localization was already described by a corresponding IPR (see Table I). They may appear either isolated or forming compounds with other dyons (dyon-dyon pairs) or antidyons (dyon-antidyon pairs), including the possibility to recombine into calorons.

IV. RESULTS OF CLUSTER ANALYSIS FOR THE QCD ENSEMBLES

In the following we will analyze our two QCD ensembles of thermalized configurations along the lines sketched above. In order to identify topological clusters of the lattice gauge fields with the help of the low-lying spectrum of the overlap operator, we used a fixed cut on eigenvalues $\lambda_{\text{sm}} = 331$ MeV for configurations with $L_s = 16$, $T = T_\chi$ (see above). For configurations with $L_s = 24$ (50 configurations at $T = 1.06T_\chi$) we take $\lambda_{\text{sm}} = 254$ MeV. In all three sectors (selected by the angles ϕ_i) the fermionic topological density is

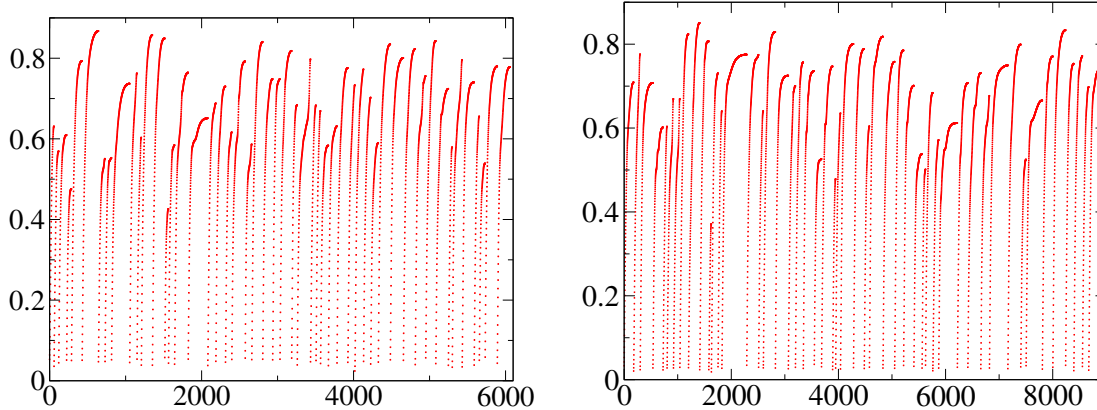


FIG. 2: The evolution of the cosine $\cos(\theta)$, the cosine of an “angle” between gluonic and fermionic topological charge density (see text), shown as function of common flow time $(\tau_O/\Delta\tau)$, consecutively for all 50 configurations of the ensemble I (left panel) and of the ensemble II (right panel).

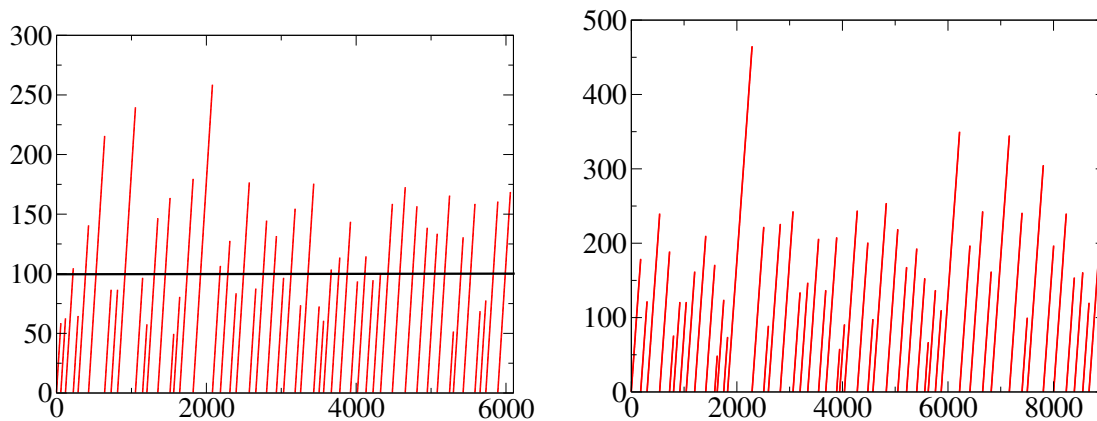


FIG. 3: The number of steps of over-improved gradient flow $(\tau_O/\Delta\tau)$ (with step size $\Delta\tau = 0.02$) growing until the cosine reaches the maximum, i. e. the best matching is achieved between the gluonic topological charge density and the fermionic topological charge density (averaged over boundary conditions). Shown for all 50 configurations of the ensemble I (left panel) and ensemble II (right panel).

constructed.

For the purpose of detecting gluonic features of (anti)dyon excitations among such clusters we have made the configurations undergo the procedure of over-improved gradient flow until the gluonic topological density profiles optimally matched the (averaged over sectors) fermionic one, analogously to what we did in our previous paper [21] where we followed the concept of an equivalent filtering as developed in [47–49]. This filtering in particular acting (smoothing) the local holonomy, while the gluonic topological density fits to the sector-averaged fermionic density, anyway, by construction.

First we have applied the same cluster analysis as in our previous paper [21] with a variable lower cutoff $q_{\text{cut}} > 0$ in order to characterize the cluster properties of the three density functions Eq. (23) in the thermal ensembles.

Let us summarize here the idea of the cluster algo-

rithm. In a first step - for each of the three fermionic boundary conditions Eq. (22) - the algorithm identifies the lattice points forming the interior of *all* clusters (the so-called “topological cluster matter”) defined by the condition $|q(x)| > q_{\text{cut}}$. The crucial second step is to enquire the connectedness between the lattice points in order to form individual extended clusters out of this “cluster matter”. Neighbouring points with $|q(x)|$ above threshold and sharing the same sign of the topological charge density are declared to belong to the same cluster. The cutoff q_{cut} has been chosen such as to resolve the given “continuous” distribution $q(x)$ into a *maximal number* of internally connected and mutually separated clusters. The cutoff value has been independently adapted for each configuration.

For ensemble I, the difference between the two cutoff values λ_{sm} is small. Between the two levels of gradient flow, the resulting number of all clusters N_{cl} coincide within errors. On the other hand, the same

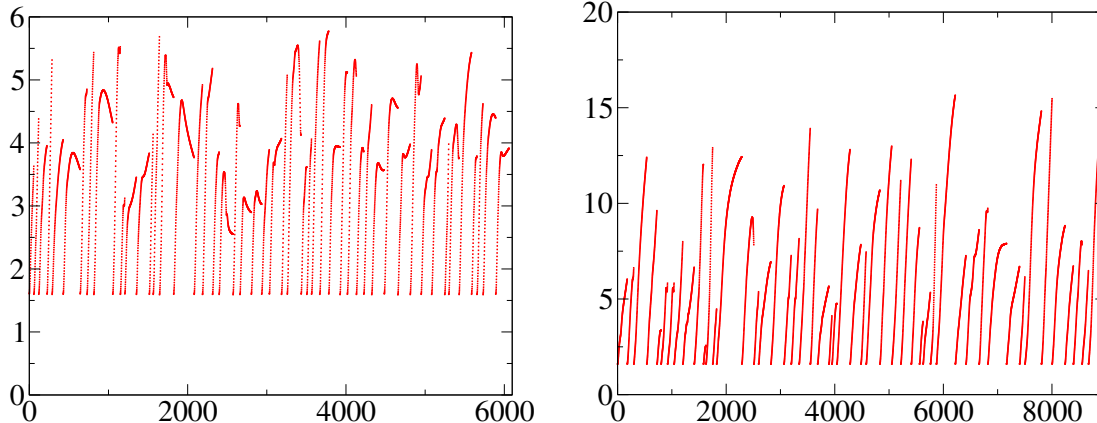


FIG. 4: The inverse participation ratio IPR evolving in the course of over-improved gradient flow ($\tau_O/\Delta\tau$) until the best matching between the gluonic topological charge density and the fermionic topological charge density (averaged over boundary conditions) is achieved. Shown for all 50 configurations of the ensemble I (left panel) and ensemble II (right panel).

cut-off $\lambda_{\text{sm}} = 254$ MeV applied to lattices with different volumes ($V_4(II)/V_4(I) = (3/2)^3/(1.06)^4 \approx 2.67$) gives us the possibility to understand the size of finite volume effects: all extensive quantities (as it can be seen from the Table I) are differing from each other by a factor of order 2.

There are two conditions to check the *dyonic nature* of isolated clusters, namely (1) an integrated topological charge close to \pm one third *and* (2) the existence of a point inside where two eigenvalues of the local holonomy become degenerate.

If the holonomy is represented by the local Polyakov loop, this second condition corresponds to a position of one point in the cluster's Weyl plot close to one of its three sides. According to the type of fermionic boundary condition applied, one can anticipate which side of the Weyl plot should be approached: the left side corresponding to antiperiodic boundary conditions ϕ_3 , the upper right side corresponding to ϕ_2 , the lower right side corresponding to ϕ_1 . Among all points belonging to a cluster we have searched for a minimum of the distance to the corresponding side of the Weyl plot. In this way we have defined which point should be considered as the “center of the cluster” (compare Fig.(6)).

In order to find the integrated topological charge of the clusters we use the gluonic topological charge density as it has appeared after applying the gradient flow process required to match the gluonic topological charge density to the fermionic one. In this case we find clusters of the gluonic topological charge density in the same way as we found before clusters of fermionic topological charge density according to three different types of fermionic boundary conditions.

If for example the extrema of the clusters of fermionic topological charge density for the first type of b.c. (with time-like monopole links inside) fall

into a cluster of gluonic topological charge, we say that this gluonic topological cluster contains a dyon of first type. The same procedure is applied to identify the character as being another type of dyons. This gives us the possibility to sort all gluonic topological clusters into the following categories: as full calorons (three different dyons inside), as 3 types of dyon pairs (two different dyons inside), as 3 types of dyons (one dyon inside), or as background (no dyons inside).

For isolated dyons and dyon pairs and for full calorons we find the integrated topological charges the same way as for isolated dyons and calorons in the case of SU(2) objects [50]. The results can be seen on Fig.(5) for the ensemble II.

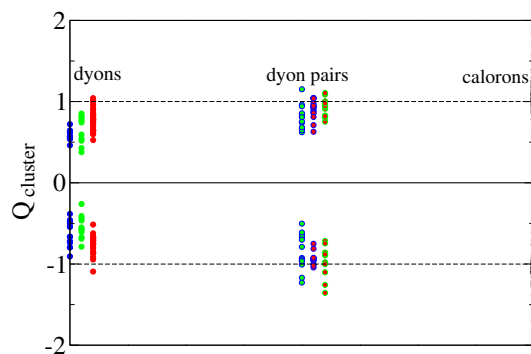


FIG. 5: The integrated topological charges of gluonic topological clusters interpreted as 3 types of dyons, 3 types of dyon pairs and full calorons (analyzed for the ensemble II). The color code refers to the type of dyons.

There is another question to be checked: correlation with the time-like currents of Abelian monopoles in the Abelian projection after MAG. This is particularly

interesting at much higher temperature where Abelian monopoles become thermal (cyclic) and almost static (exclusively timelike). Even close to the transition like in our case this might *sharpen* the test for clusters being really dyons or antidyons.

All quantitative data on the correlations between topological charge density and MAG monopole content is presented in Table II.

Our main results on the correlation of low-lying modes of the overlap Dirac operator (as represented by the clusters of fermionic topological charge) with the Abelian monopoles of MAG are as follows. For the ensemble I (ensemble II) the topological clusters occupy about 11% (8%) of the lattice 4-volume, whereas topological clusters constrained to contain static MAG monopole currents cover 10% (7%) of the lattice volume, but the latter contain about 35% (40%) of the time-like dual links carrying MAG monopoles. Inside those topological clusters which are pierced by MAG monopoles, the density of monopoles is about 5 (9) times larger than outside these clusters. These numbers become even more pronounced if one counts not just the time-like monopole currents (dual links) in topological clusters but the numbers of thermal monopoles piercing topological clusters. Around 75% (60%) of thermal (thermally winding) monopoles are seen piercing topological clusters.

We expect that the topological clusters detected with antiperiodic boundary conditions (in our case with a real-valued average Polyakov loop) can be viewed as related to more heavy dyons: at the higher temperature $T = 1.06T_\chi$ (in the ensemble II) they are expected to become statistically suppressed because of their higher action in comparison with the other constituents of a caloron. We can estimate this suppression quantitatively by measuring the abundance of thermal monopoles piercing topological clusters of third type compared to those piercing topological clusters of first or second type. Such thermal monopoles, if they are correlated with clusters of topological charge, we are inclined to associate with physical dyons. We found the proportion 9.9 : 10.6 : 6.7 (see the lower subtable). Thus, the heavier caloron constituent clusters are really suppressed already when the temperature is exceeding T_χ by only few percent.

Furthermore, the correlation between the local Polyakov loop on one side and the dyon nature of clusters of topological charge on the other is increased if the clusters are constrained to be coinciding with Abelian monopoles. The Polyakov loop tests the degeneracy of holonomy eigenvalues in the cluster centers which are (by our definition above) distinguished among all the cluster points by the condition to have a minimal distance from the sides of the Weyl plot.

We show the scatter plot of local Polyakov loops measured in the centers of those clusters which are

associated with magnetic monopoles. Since the clusters are labelled (see the color code) by one of the three boundary conditions for the fermionic modes (used to define the fermionic topological charge density), the scatter plot over the Weyl plot Fig. 6 shows the different regions of population. The tendency of the Polyakov loop in the cluster centers to concentrate along the corresponding sides of the Weyl plot is much more pronounced than it was for all clusters (corresponding picture before). We remind that the Polyakov loop is measured for the gluonic field that has emerged from gradient flow at maximal matching of gluonic and fermionic topological densities.

V. CONCLUSIONS

For lattice QCD we have discussed the dyonic signatures of clusters of topological charge selected by three types of temporal boundary conditions applied to the overlap modes used in the fermionic definition of topological density. In contrast to our previous paper on $SU(3)$ gluodynamics [22] here for the construction of fermionic topological densities not the number of pairs of near-zero modes is fixed but the eigenvalue cutoff. The thermal lattice gauge fields were generated close to the crossover temperature. Topological clusters to be considered as candidates to be dyons were established by filtering, i.e. restricting to low-lying modes of the overlap Dirac operator with specific boundary conditions. Additionally, we have applied to the gluonic lattice fields the procedure of overimproved gradient flow (instead of overimproved cooling in [22]) after which a similar pattern of clusters occurs within the gluonic topological charge distribution (however averaged over boundary conditions). We looked for distributions of local Polyakov loop and searched for MAG monopole currents in the gradient-flow-smearred gluonic fields. We found clear correlations of the topological clusters with thermal monopoles as well as with lattice sites, where the local holonomy has close-to-degenerate eigenvalues. All this points to the correctness of an interpretation in terms of (anti)dyon excitations of the KvBLL type and has enabled us to estimate corresponding densities and cluster properties.

Acknowledgments

B.V.M. appreciates the support of Humboldt-University of Berlin where the main part of the work was done. He also has been supported by the grants RFBR 13-02-01387a, 15-02-07596a. E.-M.I. and M.M.-P. acknowledge financial support by the Heisenberg-Landau Program between the German BMBF and BLTP of JINR Dubna.

Clusters obtained with lowest overlap modes for $16^3 \times 8$ configurations

Type of clusters	V_{cl}	V_{clmon}	N_{cl}	N_{clmon}	N_{mon}	N_{moncl}	N_{loop}	N_{loopcl}
1-st type clusters	6.7(8)%	6.1(8)%	12.9(3)	3.5(2)	—	32(3)	—	5.4(4)
2-nd type clusters	6.0(7)%	5.2(7)%	13.1(3)	3.7(2)	—	30(2)	—	5.4(4)
3-d type clusters	6.1(8)%	5.5(8)%	12.0(4)	3.6(2)	—	31(2)	—	5.1(4)
All clusters ($\lambda_{sm} = 331$ MeV)	11(1)%	10(1)%	38(1)	10.8(6)	129(4)	45(3)	8.7(5)	6.4(4)
All clusters ($\lambda_{sm} = 254$ MeV)	12(1)%	11(1)%	32(1)	9.6(6)	120(4)	42(3)	8.1(5)	5.8(4)

Clusters obtained with lowest overlap modes for $24^3 \times 8$ configurations

Type of clusters	V_{cl}	V_{clmon}	N_{cl}	N_{clmon}	N_{mon}	N_{moncl}	N_{loop}	N_{loopcl}
1-st type clusters	5.1(3)%	4.4(4)%	24(1)	5.8(3)	—	59(3)	—	9.9(6)
2-nd type clusters	6.2(6)%	5.5(6)%	24(1)	5.5(3)	—	64(4)	—	10.6(7)
3-d type clusters	1.8(2)%	1.5(2)%	11(1)	5.7(4)	—	40(3)	—	6.7(6)
All clusters ($\lambda_{sm} = 254$ MeV)	8.0(6)%	7.0(6)%	59(2)	17.0(8)	193(8)	76(5)	20.2(8)	12.1(7)

TABLE II: Results of the cluster analysis using low-lying overlap operator modes with three kinds of boundary conditions. All numbers indicate averages per configuration. The pure statistical errors are given in parentheses. We denote with V_{cl} - the volume fraction occupied by all topological clusters, $V_{cl\ mon}$ - the volume fraction occupied by clusters identified to contain time-like magnetic monopoles, N_{cl} - the number of all clusters per configuration, $N_{cl\ mon}$ - the number of clusters identified to contain time-like magnetic monopoles, N_{mon} - the overall number of dual timelike links carrying monopole currents, $N_{mon\ cl}$ - the number of dual timelike links carrying monopole currents found inside topological clusters, N_{loop} - the overall number of thermally closed monopole worldlines, $N_{loop\ cl}$ - the number of thermally closed monopole worldlines piercing topological clusters. The first part of the table is related to the ensemble I ($L_s = 16$ at $T = T_\chi$). Here we show the effect of changing the cut-off from $\lambda_{sm} = 331$ MeV (derived for 20 eigenmodes) to a smaller cut-off $\lambda_{sm} = 254$ MeV (implying more iterations of gradient flow). The second part of the table is related to the ensemble II ($L_s = 24$ at $T = 1.06T_\chi$), where the cut-off $\lambda_{sm} = 254$ MeV (derived for 30 eigenmodes) has been applied.

-
- [1] T. C. Kraan and P. van Baal, Nucl.Phys. **B533**, 627 (1998), hep-th/9805168.
- [2] T. C. Kraan and P. van Baal, Phys.Lett. **B435**, 389 (1998), hep-th/9806034.
- [3] K.-M. Lee and C.-H. Lu, Phys.Rev. **D58**, 025011 (1998), hep-th/9802108.
- [4] A. M. Polyakov, Nucl. Phys. **B120**, 429 (1977).
- [5] B. Martemyanov and S. Molodtsov, JETP Lett. **65**, 142 (1997).
- [6] P. Gerhold, E.-M. Ilgenfritz, and M. Müller-Preussker, Nucl. Phys. **B760**, 1 (2007), hep-ph/0607315.
- [7] D. Diakonov and V. Petrov, Phys.Rev. **D76**, 056001 (2007), 0704.3181.
- [8] F. Bruckmann, S. Dinter, E.-M. Ilgenfritz, B. Maier, M. Müller-Preussker, and M. Wagner, Phys.Rev. **D85**, 034502 (2012), 1111.3158.
- [9] E. Shuryak, J. Phys. **G39**, 054001 (2012), 1112.2573.
- [10] P. Faccioli and E. Shuryak, Phys. Rev. **D87**, 074009 (2013), 1301.2523.
- [11] R. Larsen and E. Shuryak (2014), 1408.6563.
- [12] Y. Liu, E. Shuryak, and I. Zahed (2015), 1503.03058.
- [13] Y. Liu, E. Shuryak, and I. Zahed (2015), 1503.09148.
- [14] R. Larsen and E. Shuryak (2015), 1504.03341.
- [15] M. Garcia Perez, A. Gonzalez-Arroyo, C. Pena, and P. van Baal, Phys.Rev. **D60**, 031901 (1999), hep-th/9905016.
- [16] M. N. Chernodub, T. C. Kraan, and P. van Baal, Nucl. Phys. Proc. Suppl. **83**, 556 (2000), hep-lat/9907001.
- [17] C. Gattringer, Phys. Rev. **D67**, 034507 (2003), hep-lat/0210001.
- [18] C. Gattringer and S. Schaefer, Nucl. Phys. **B654**, 30 (2003), hep-lat/0212029.
- [19] V. Bornyakov, E.-M. Ilgenfritz, B. Martemyanov, S. Morozov, M. Müller-Preussker, and A. Veselov, Phys.Rev. **D76**, 054505 (2007), 0706.4206.
- [20] V. Bornyakov, E.-M. Ilgenfritz, B. Martemyanov, and M. Müller-Preussker, Phys.Rev. **D79**, 034506 (2009), 0809.2142.
- [21] E.-M. Ilgenfritz, B. Martemyanov, and M. Müller-Preussker, Phys.Rev. **D89**, 054503 (2014), 1309.7850.
- [22] V. G. Bornyakov, E. M. Ilgenfritz, B. V. Martemyanov, and M. Muller-Preussker, Phys. Rev. **D91**, 074505 (2015), 1410.4632.
- [23] V. Bornyakov et al. (DIK Collaboration), Phys.Rev. **D71**, 114504 (2005), hep-lat/0401014.
- [24] V. Bornyakov, R. Horsley, S. Morozov, Y. Nakamura, M. Polikarpov, et al., Phys.Rev. **D82**, 014504 (2010), 0910.2392.

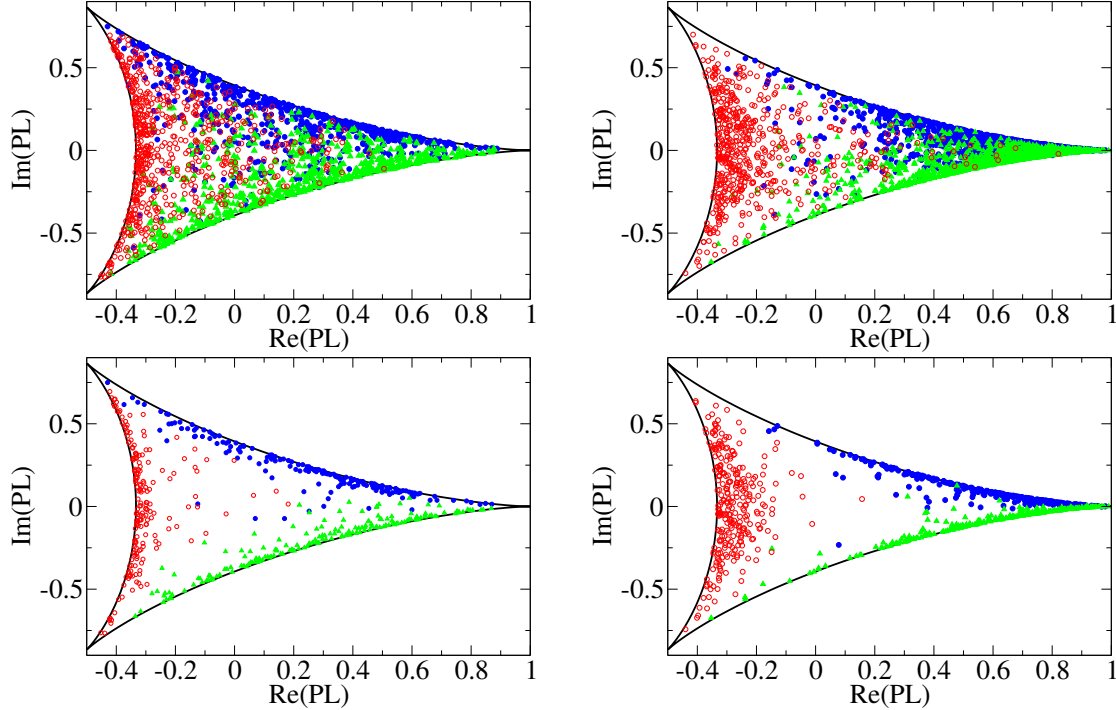


FIG. 6: Scatter plots of Polyakov loop PL (for configurations having undergone the over-improved gradient flow procedure) in the centers of all clusters (upper row) and of clusters selected to contain monopoles (lower row). The clusters are separated according to the type of boundary condition for the overlap near-zero modes. For clusters of first type the Polyakov loop is shown by green triangles, for clusters of second type - by blue filled circles, for clusters of third type - by red open circles. This scatter plots show all clusters of all 50 configurations of size $L_s = 16$ and $T = T_\chi$ on the left (ensemble I) and size $L_s = 24$ and $T = 1.06T_\chi$ on the right (ensemble II).

- [25] Y. Nakamura and H. Stüben, PoS **LATTICE2010**, 040 (2010), 1011.0199.
- [26] K. Jansen and R. Sommer (ALPHA collaboration), Nucl.Phys. **B530**, 185 (1998), hep-lat/9803017.
- [27] M. Gockeler, R. Horsley, A. C. Irving, D. Pleiter, P. E. L. Rakow, G. Schierholz, H. Stuben, and J. M. Zanotti, Phys. Rev. **D73**, 054508 (2006), hep-lat/0601004.
- [28] V. Bornyakov, E.-M. Ilgenfritz, B. Martemyanov, V. Mitrjushkin, and M. Müller-Preussker, Phys.Rev. **D87**, 114508 (2013), 1304.0935.
- [29] A. S. Kronfeld, G. Schierholz, and U. J. Wiese, Nucl. Phys. **B293**, 461 (1987).
- [30] F. Brandstater, U. J. Wiese, and G. Schierholz, Phys. Lett. **B272**, 319 (1991).
- [31] W. W. Tucker and J. D. Stack, Nucl. Phys. Proc. Suppl. **106**, 643 (2002), [643(2001)], hep-lat/0110165.
- [32] C. Bonati and M. D’Elia, Nucl. Phys. **B877**, 233 (2013), 1308.0302.
- [33] G. S. Bali, V. Bornyakov, M. Müller-Preussker, and K. Schilling, Phys. Rev. **D54**, 2863 (1996), hep-lat/9603012.
- [34] V. Bornyakov, G. Schierholz, and T. Streuer, Nucl. Phys. Proc. Suppl. **106**, 676 (2002), [676(2001)], hep-lat/0111018.
- [35] V. G. Bornyakov et al. (DIK), Phys. Rev. **D70**, 074511 (2004), hep-lat/0310011.
- [36] S. O. Bilson-Thompson, D. B. Leinweber, and A. G. Williams, Ann. Phys. **304**, 1 (2003), hep-lat/0203008.
- [37] M. Luscher, Commun. Math. Phys. **293**, 899 (2010), 0907.5491.
- [38] M. Lüscher, JHEP **1008**, 071 (2010), 1006.4518.
- [39] M. Luscher and P. Weisz, JHEP **02**, 051 (2011), 1101.0963.
- [40] M. Garcia Perez, A. Gonzalez-Arroyo, J. R. Snippe, and P. van Baal, Nucl.Phys. **B413**, 535 (1994), hep-lat/9309009.
- [41] C. Bonati and M. D’Elia, Phys. Rev. **D89**, 105005 (2014), 1401.2441.

- [42] P. H. Ginsparg and K. G. Wilson, Phys. Rev. **D25**, 2649 (1982).
- [43] H. Neuberger, Phys. Lett. **B417**, 141 (1998), hep-lat/9707022.
- [44] H. Neuberger, Phys. Lett. **B427**, 353 (1998), hep-lat/9801031.
- [45] P. Hasenfratz, V. Laliena, and F. Niedermayer, Phys. Lett. **B427**, 125 (1998), hep-lat/9801021.
- [46] H. Neff, N. Eicker, T. Lippert, J. W. Negele, and K. Schilling, Phys. Rev. **D64**, 114509 (2001), hep-lat/0106016.
- [47] F. Bruckmann, C. Gatttringer, E.-M. Ilgenfritz, M. Müller-Preussker, A. Schäfer, and S. Solbrig, Eur.Phys.J. **A33**, 333 (2007), hep-lat/0612024.
- [48] E.-M. Ilgenfritz, D. Leinweber, P. Moran, K. Koller, G. Schierholz, et al., Phys.Rev. **D77**, 074502 (2008), 0801.1725.
- [49] F. Bruckmann, F. Gruber, C. Lang, M. Limmer, T. Maurer, A. Schäfer, and S. Solbrig, PoS **CONFINEMENT8**, 045 (2008), 0901.2286.
- [50] E.-M. Ilgenfritz, B. Martemyanov, M. Müller-Preussker, and A. Veselov, Phys.Rev. **D71**, 034505 (2005), hep-lat/0412028.
- [51] In contrast to gradient flow, cooling has no adaptable “flow time step” $\Delta\tau$ and consists of sequential minimizations with respect to single links swept through the lattice. In the case of $SU(3)$ this requires a non-analytical operation called “projection to the group”.
- [52] diffusion length given in lattice units a